

Reports

Slip Deficit on the San Andreas Fault at Parkfield, California, as Revealed by Inversion of Geodetic Data

PAUL SEGALL AND RUTH HARRIS

A network of geodetic lines spanning the San Andreas fault near the rupture zone of the 1966 Parkfield, California, earthquake (magnitude $M = 6$) has been repeatedly surveyed since 1959. In the study reported here the average rates of line-length change since 1966 were inverted to determine the distribution of interseismic slip rate on the fault. These results indicate that the Parkfield rupture surface has not slipped significantly since 1966. Comparison of the geodetically determined seismic moment of the 1966 earthquake with the interseismic slip-deficit rate suggests that the strain released by the latest shock will most likely be restored between 1984 and 1989, although this may not occur until 1995. These results lend independent support to the earlier forecast of an $M = 6$ earthquake near Parkfield within 5 years of 1988.

SINCE 1857 FIVE EARTHQUAKES OF magnitude $M = 6$ have occurred on the 30-km-long Parkfield, California, segment of the San Andreas fault, the latest on 27 June 1966. On the basis of an extrapolation of the historical earthquake sequence, which has a mean repeat time of 21.9 ± 3.1 years, it has been forecast that the next Parkfield earthquake will occur in 1988 ± 5 years (1). Recently, however, possible errors in the locations of earthquakes prior to 1922 have led some workers to question the regular recurrence of past Parkfield earthquakes (2).

A network of geodetic lines spanning the fault near Parkfield has been repeatedly surveyed with precise distance-measuring instruments since 1959. We used the results of these surveys (observed changes in line lengths) to constrain the distribution of fault slip at depth. A unique aspect of the Parkfield data set is that the measurements span virtually a complete earthquake cycle, from before the 1966 earthquake to the present. This allows a comparison of the strain accumulation since 1966 with the strain released in the 1966 sequence. The results of this comparison provide a test of the potential for an $M = 6$ earthquake in the Parkfield area by 1988, a test that is independent of the periodicity, or aperiodicity, of the earthquake sequence before 1966.

A total of 13 baselines in the Parkfield area were surveyed before the 1966 earthquake (3); subsequently the network has been expanded to more than 80 baselines (4, 5). In this study, we used only the 45 frequently surveyed lines illustrated in Fig. 1 (6). Repeated measurements of these lines were analyzed to determine average rates of baseline extension or contraction during the interseismic period (1966 to 1984), as well

as the coseismic changes in length of the 13 baselines measured before the 1966 earthquake.

The Parkfield segment of the San Andreas fault is bounded on the northwest by an aseismically slipping, or creeping, zone and on the southeast by a nonslipping, or locked, zone that last ruptured during the 1857 Fort Tejon $M = 8$ earthquake. The average rate of shallow fault slip measured by an array of instruments, including creepmeters, alignment arrays, and short-aperture trilateration networks (7-10), decreases monotonically from nearly 30 mm year⁻¹ in the creeping zone northwest of the 1966 epicenter to zero in the locked zone south of the 1966 rupture (Fig. 2).

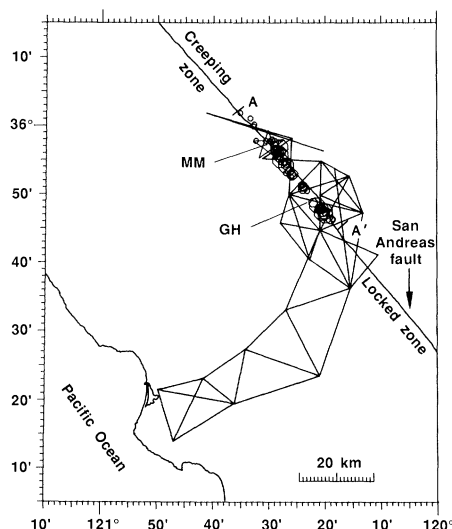


Fig. 1. Parkfield trilateration network. Straight lines represent geodetic survey lines used in interseismic slip rate inversion; 1966 Parkfield main shock (star) and $M > 2$ aftershocks (circles) (24); MM, Middle Mountain; GH, Gold Hill. A-A' indicates the cross section shown in Figs. 2 and 3.

We postulate that the observed changes in baseline length are caused by some distribution of strike-slip on the San Andreas fault, plus a small component of random survey error. The fault is modeled as a planar surface of displacement discontinuity in a homogeneous, isotropic, elastic half-space. The expected changes in baseline lengths due to general fault-slip distributions can then be calculated from elastic dislocation theory (11, 12). In this study, the fault-slip distribution is approximated by a discrete array of rectangular elements with uniform slip (dislocations). At seismogenic depths, the 36-km-long model Parkfield fault segment is divided into elements 3 km long by 2 km deep. Below a specified depth, referred to as the transition depth, the fault is represented by a single semi-infinite dislocation. The slip rate below the transition depth is thus taken to be spatially uniform. Parameterizing the fault slip in this fashion allows the baseline changes to be expressed as linear functions of the unknown slip rates (12).

Shallow fault-slip data are incorporated into the analysis by requiring that the slip rate in the near-surface layer fit the surface creep rate profile shown in Fig. 2 (13). To simulate the effect of the creeping zone, we fixed the slip rate northwest of the Parkfield segment at 25 mm year⁻¹ from the surface to the transition depth (14). Southeast of the Parkfield segment, the fault is locked from the surface to the transition depth.

To estimate the unknown slip rates from the known rates of baseline change we used a variation of the "natural" or "generalized" inverse (15, 16). That part of the slip rate distribution that is overdetermined by the data is found by least squares, while the underdetermined part is specified by the assumption that the slip rate distribution is, to some degree, smooth. The inverse operator is thus chosen to minimize the weighted sum of the squares of residuals in the "data space" while at the same time minimizing the roughness of the slip distribution in the "model space" (16, 17). Separation of the overdetermined and underdetermined parts of the slip rate distribution is accomplished through a singular-value decomposition (15, 16). Increasing the number of singular values used in constructing the inverse operator improves the data fit while increasing the roughness and variance of the slip rate distribution.

We performed an initial series of inversions, varying the transition depth, to determine the dependence of the deep-slip rate on the transition depth (18). The results demonstrated that transition depths be-

U.S. Geological Survey, Menlo Park, CA 94025.

tween 14 and 22 km fit the data equally well; however, the estimated deep-slip rate increases with transition depth (Table 1). A deep-slip rate close to 33 mm year⁻¹ is consistent with the current rate of rigid-block motion in the creeping zone northwest of the Parkfield segment and with the late Holocene slip rate southeast of Parkfield (19).

Figure 3 illustrates the slip rate patterns for a series of inversions, with a transition depth of 22 km and a deep-slip rate fixed at 33 mm year⁻¹. In Fig. 3a, the number of singular values in the inversion equals the number of constrained elements (20). This solution fits the observed creep profile, minimizes the roughness of the slip rate pattern, and is thus, in some sense, the smoothest model of the transition between the creeping and locked zones. Despite its simplicity and the fact that the smooth model (Fig. 3a) reproduces the gross features of the deformation pattern (21), significant improvements in the data fit can be achieved by increasing the number of independent parameters in the inversion.

The model with one additional degree of freedom (singular value) is shown in Fig. 3b. Improvement in the fit to the trilateration data (Table 2) is achieved by reducing the slip rate relative to the smooth model. In this case, the southern 20 km of the Parkfield segment is locked, or nearly locked, at intermediate depths. Adding another degree of freedom to the model results in the slip rate profile shown in Fig. 3c. The improvement in data fit is achieved primarily by extending the locked zone northwestward to Middle Mountain. Examination of the model residuals suggests that addition of the first two degrees of freedom significantly improves the fit to the geodetic data, whereas the effect of adding the third is insignificant (Table 2). The geodetic data are thus capable of determining only three linearly independent characteristics of the slip distribution, of which the third is the deep-slip rate (22).

The residuals to the preferred strike-slip model exhibit a pattern indicating uniaxial shortening perpendicular to the strike of the San Andreas fault. Including uniform strain normal to the fault trend as a parameter in the model and adding a corresponding degree of freedom to the inverse improves the fit appreciably without altering the predicted fault-slip pattern or the moment rate (Table 2). Shortening normal to the fault has been recognized from the orientation of fold axes and earthquake focal mechanisms in the central California Coast Ranges and is predicted by global plate motion models (23) but had previously not been detected geodetically.

Table 1. Transition depth and deep-slip rate.

Transition depth (km)	Deep-slip rate (mm year ⁻¹)
14	25.5
16	27.3
18	29.1
20	30.9
22	32.7

One can best judge the quality of the model fit to the geodetic data by comparing the station velocities calculated directly from an adjustment of the distance measurements with the velocities predicted by the inverse model. Velocity vectors can be calculated for 17 of the 22 geodetic stations in the network (Fig. 4). For all 17 stations the predicted velocities are consistent with the observed motions at the level of 2 SD. The average residual from the network adjustment (1.00 mm year⁻¹) provides a model-independent measure of the inherent errors

in the baseline rates of change. In comparison, the model including both fault slip and strain normal to the fault has an average residual of 1.09 mm year⁻¹.

Inversions with transition depths ranging from 14 to 20 km exhibit locked or slowly slipping zones similar to those shown in Fig. 3c. This result, in combination with an analysis of the model resolution (16), demonstrates that the data can be used to detect the presence of a locked zone but cannot resolve details of its location or shape. In particular, the depth to the bottom of the locked zone is poorly resolved. Considering the resolution of the data, the locked zone predicted by the inversions coincides quite closely with the rupture surface of the 1966 earthquake as delineated by its aftershocks (24). The hypocenter of the main shock is located at the northwest end of the locked zone, and the aftershocks extend some 30 km southeastward into the zone of negligible interseismic slip (Fig. 3c). For transition depths greater than 14 km the locked zone

Fig. 2. Shallow fault-slip rate versus distance along fault, showing average slip rate as measured by creepmeters (circles), alignment arrays (squares), and short-baseline trilateration networks (triangles). Vertical error bars represent the range of slip estimates (10); horizontal error bars indicate the locations of short-baseline trilateration networks. The heavy line shows the shallow fault-slip rate profile used in interseismic inversions.

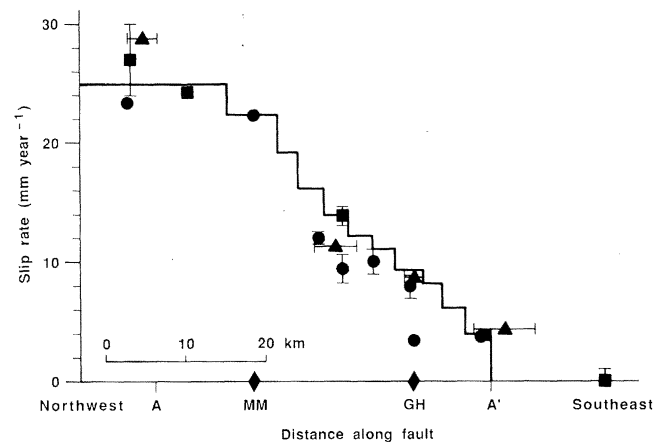


Table 2. Model fits to geodetic data.

Model	Number of singular values*	Misfit† (mm year ⁻¹)	Moment rate (×10 ²⁴ dyne-cm year ⁻¹)	Normal strain (ppm year ⁻¹)	Figure
Fault slip	0	1.64	4.5	0.0‡	3a
Fault slip	1	1.32	2.7	0.0‡	3b
Fault slip	2	1.24	2.5	0.0‡	3c
Fault slip	3	1.25	2.5	0.0‡	Not shown
Fault slip plus normal strain	3	1.09	2.6	-0.06	Not shown

*Exclusive of singular values that correspond to constraints.

†The weighted root mean square (rms) misfit is given by $\left[\frac{1}{N-P} \sum_{i=1}^N r_i^2 w_i^2 \right]^{1/2}$

where the residual $r_i = o_i - c_i$ is the difference between the observed rate of baseline change, o_i , and the calculated rate, c_i ; $N = 45$ is the number of baselines; and P is the number of independent parameters (equal to the number of singular values). The residuals are weighted by the reciprocal of the variance normalized by the weighted average of the variances $w_i^2 = (\bar{\sigma}/\sigma_i)^2$ where σ_i^2 is the variance in the i th baseline rate of change, and $\bar{\sigma}^2$ is the average variance given by $\bar{\sigma}^2 = \frac{1}{N} \sum_{i=1}^N (1/\sigma_i)^2$. For this data set $\bar{\sigma} = 0.80$ mm year⁻¹. These misfits can be compared to the rms misfit of the network adjustment, 1.00 mm year⁻¹, which measures the pure error in the data arising from inconsistencies in the baseline rates of change.

‡The uniform normal strain in these models is assumed to be zero.

extends to greater depth than the aftershocks (Fig. 3c), implying substantial aseismic afterslip below the aftershock zone.

We inverted the coseismic changes in the length of the 13 lines measured before and after the 1966 earthquake to determine the event's seismic moment, using the same inversion procedure described above. Because the geodetic measurements do not adequately constrain the depth of seismic slip, we assume in the following analysis that no coseismic or postseismic slip occurred below the transition depth and allow this parameter to vary from 14 to 22 km. The fact that aftershocks in 1966 occurred to depths of 14 km (24) demonstrates slip to at least that depth. The 1966 seismic moment estimated from the geodetic data ranges from 5.5×10^{25} dyne-cm, if we assume no slip below 14 km, to 9.1×10^{25} dyne-cm, if we assume no slip below 22 km. These estimates exceed the seismic moment of 0.9×10^{25} to 2.1×10^{25} dyne-cm calculated from surface waves (25). Because surveys were not conducted until several weeks or more after the earthquake, the geodetically determined seismic moment includes an unknown amount of aseismic afterslip. Comparison with similar earthquakes in California suggests that postseismic slip can account for a factor of 2 increase in seismic moment (26). The remaining discrepancy between the surface wave and geodetic moments may be an artifact of the smoothing in the inversion, which tends to introduce substantial slip at depth where the network has poor resolution. An alternative inversion procedure that tends to minimize the slip (27) yields a moment of 3.2×10^{25} dyne-cm, which we take to be a lower bound on the 1966 moment.

We used these results to calculate the time required for a moment deficit equal to the 1966 seismic moment to accumulate. This should be equivalent to the recurrence time according to the time-predictable earthquake recurrence model (28). We considered two limiting models, model 1 with a transition depth at 14 km and model 2 with a transition depth at 22 km (29). In each case, the slip deficit relative to the corresponding deep-slip rate was used to calculate a moment deficit rate. We then compared

Fig. 3. Interseismic slip rate pattern for a transition depth of 22 km and a deep-slip rate of 33 mm year⁻¹. Colors indicate slip rate in millimeters per year. (a) Smooth model. (b) Same as (a) but with one additional degree of freedom in the inversion. (c) Same as (a) but with two additional degrees of freedom. The longitudinal cross section of 1966 aftershocks (circles) and mainshock (star) projected onto the model fault plane (24) outlines the rupture surface of the 1966 Parkfield earthquake.

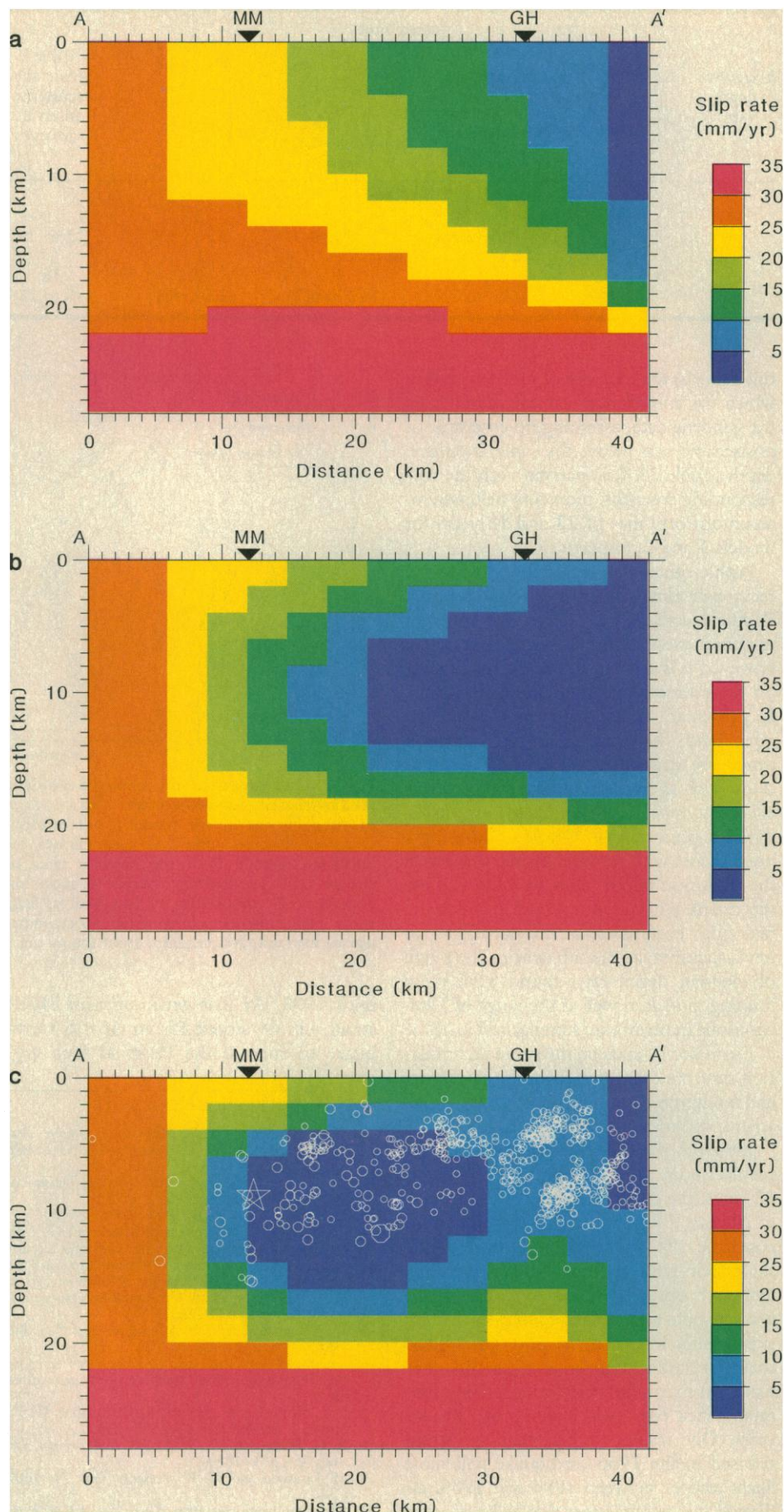


Table 3. Time-predictable recurrence estimates. Numbers in parentheses are ranges.

Transition depth (km)	Deep-slip rate (mm year ⁻¹)	Interseismic		Coseismic moment (×10 ²⁵ dyne-cm)	Time-predictable recurrence interval (years)
		Moment rate (×10 ²⁴ dyne-cm year ⁻¹)	Moment-deficit rate (×10 ²⁴ dyne-cm year ⁻¹)		
14	25.5	Model 1		5.5 (3.2 to 5.5)	23 (11 to 29)
		1.5 (0.9 to 2.0)	2.4 (1.9 to 3.0)		
22	32.7	Model 2		9.1 (3.5 to 9.1)	18 (5 to 22)
		2.5 (1.1 to 3.7)	5.2 (4.1 to 6.7)		

this value to the moment of the 1966 event, which for consistency was calculated from the geodetic data, assuming no coseismic or postseismic slip below the same transition depth (Table 3). Comparison with the corresponding coseismic moments yields strain-accumulation times of 23 and 18 years for models 1 and 2, respectively.

Both estimates are reasonably close to the recurrence time (of 22 ± 3 years) for past Parkfield earthquakes. Given the inherent nonuniqueness in the geodetic inversions, however, it is difficult to place error bounds on the estimated strain-accumulation time. In particular, the estimated moment deficit rates, and therefore strain accumulation times, are dependent on a priori assumptions, such as smoothing. We explored this effect by repeating the inversions, using different prior models (30, 31). Choosing a prior model with no interseismic slip above the transition depth tends to maximize the slip deficit, while a prior model in which the fault slips everywhere at the deep-slip rate tends to minimize the slip deficit. The range of moment deficit rates found from these limiting models as well as the range of 1966 coseismic moments are summarized in Table 3. Estimated bounds on the strain accumulation time are calculated from the maximum and minimum coseismic moments and interseismic moment deficit rates.

Although the preferred (smooth) models predict strain accumulation times of 18 to 23 years, the data admit intervals of from 5 to 29 years. Limiting models with minimum coseismic slip and maximum interseismic slip-deficit rates are qualitatively inconsistent with observed seismicity patterns and predict strain accumulation intervals that are significantly less than the 20+ years since the latest Parkfield earthquake. On the other hand, the maximum coseismic slip and minimum deficit rates yield intervals of 22 to 29 years. Our results suggest that the strain released in the 1966 earthquake will most likely recover between 1984 and 1989, although it is possible that this will not occur

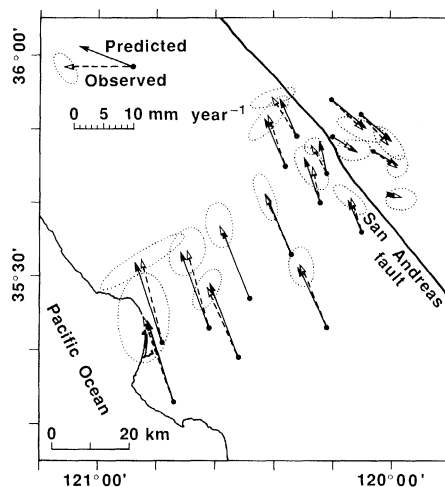


Fig. 4. Comparison of the observed geodetic station velocities (dashed vectors) with velocities predicted by the inverse model (solid vectors). Observed velocities, with 2 SD error ellipses, are calculated directly from the baseline rates of change (32). The predicted motions, including both strike-slip motion on the San Andreas fault and a small component of contraction perpendicular to the fault, are calculated from the model.

until 1995. At that time sufficient elastic strain will be stored for an $M = 6$ earthquake to rupture the Parkfield fault segment.

REFERENCES AND NOTES

1. W. H. Bakun and T. V. McEvilly, *J. Geophys. Res.* **89**, 3051 (1984); W. H. Bakun and A. G. Lindh, *Science* **229**, 619 (1985).
2. T. R. Toppozada, *Trans. Am. Geophys. Union* **66**, 982 (1985); C. R. Real, *ibid.*, p. 982.
3. *Calif. Dep. Water Resour. Bull.* **116-6** (1968).
4. The California Department of Mines and Geology took over the network from the California Department of Water Resources in 1970 and expanded the network in the Parkfield region to 32 lines (5). In the late 1970's, the U.S. Geological Survey expanded the network to 80 lines.
5. J. H. Bennet, *Calif. Div. Mines Geol. Spec. Rep.* **140** (1980).
6. Of the 45 lines analyzed, 44 were surveyed more than three times and 40 were surveyed five or more times.
7. S. S. Schulz, G. M. Mavko, R. O. Burford, W. D. Stuart, *J. Geophys. Res.* **87**, 6977 (1982).
8. R. O. Burford and P. W. Harsh, *Bull. Seismol. Soc. Am.* **70**, 1233 (1980).
9. M. Lisowski and W. H. Prescott, *ibid.* **71**, 1607 (1981).
10. Slip rates from creepmeters are averages of least

squares fits and simple end-point averages for all data before 1980 (7). Slip rates calculated from alignment arrays are averages of block-fit and end-point rates (8). In both cases, error bars encompass both estimates. Slip rates from short-aperture geodetic nets are weighted means of fault-crossing lines (9).

11. M. A. Chinnery, *Bull. Seismol. Soc. Am.* **51**, 335 (1961).
12. The change in the i th baseline length $\Delta \ell_i$ is related to fault slip $s(\zeta)$ by

$$\Delta \ell_i = \int_A G(x_i, \zeta) s(\zeta) d\zeta$$

where x_i denotes the position of the baseline end points and ζ denotes position on the fault surface A . Discretizing the slip allows the above expression to be approximated by

$$\Delta \ell = Gs$$

where $\Delta \ell$ is the vector of $N = 45$ observations, and s is the vector of M unknowns ($M > N$). The $N \times M$ matrix of coefficients G is calculated from the displacement equations given by Chinnery (11) and the relation between end-point displacements and change in baseline length [W. Thatcher, *J. Geophys. Res.* **89**, 2283 (1979)].

13. The average shallow fault-slip rates (creep rates) are appended to the linear system of equations relating the data to fault slip. The creep data are weighted more heavily than the trilateration data, which effectively constrains the solution to fit the observed shallow slip rates.
14. Slip rates of 25 to 30 mm year⁻¹ in the creeping zone northwest of the Parkfield segment are consistent with the limited fault-creep data (7-9).
15. C. Lanczos, *Linear Differential Operators* (Van Nostrand-Reinhold, Princeton, NJ, 1961); K. Aki and P. G. Richards, *Quantitative Seismology: Theory and Methods* (Freeman, San Francisco, 1980).
16. W. Menke, *Geophysical Data Analysis: Discrete Inverse Theory* (Academic Press, New York, 1984).
17. The roughness of the slip-rate distribution is quantified by

$$\sum_{i=1}^M (\nabla^2 s_i)^2$$

where

$$\nabla^2 = \frac{\partial^2}{\partial x^2} + \frac{\partial^2}{\partial z^2}$$

is the Laplacian operator (in practice, a finite-difference approximation to ∇^2 is used); x and z are, respectively, horizontal and vertical distances along the fault plane; s_i is the slip in the i th element; and M is the total number of elements. It is easily shown (16) that the inverse that minimizes the solution roughness is a weighted form of the generalized inverse that minimizes the solution length

$$\sum_{i=1}^M (s_i)^2$$

18. For each transition depth we calculated a sequence of inversions, including different numbers of singular values. The 13 constraint equations, corresponding to slip in the 12 shallow elements and the creeping zone, are heavily weighted so that including 13 singular values in the inverse merely satisfies the constraint equations, that is, the creep data. For all transition depths significant improvements in the data fit occurred with the inclusion of the 14th, 15th, and 16th singular values. Including additional singular values did not significantly improve the data fit or alter the estimated deep-slip rate. The deep-slip rates in Table 1 are estimated from inversions with 16 total singular values.
19. Thatcher (12) estimated the rate of block motion in the central creeping zone to be 33 ± 1 mm year⁻¹. K. E. Sieh and R. H. Jahns [*Geol. Soc. Am. Bull.* **95**, 883 (1984)] determined an average slip rate of 33.9 ± 2.9 mm year⁻¹ for the past 3700 years from offset stream channels.
20. Constraining the deep-slip rate increases the number of constraint equations to 14. Since the constraint equations are heavily weighted, the solution found by including the first 14 singular values simply satisfies the constraint equations.
21. W. F. Slawson and J. C. Savage, *Bull. Seismol. Soc. Am.* **73**, 1407 (1983).
22. The preferred strike-slip model (Fig. 3c) includes 16 singular values, 13 of which satisfy the creep data.

The trilateration data allow three additional linearly independent components (eigenvectors) of the slip to be resolved. Excluding the remaining singular values and their associated eigenvectors from the inverse operator tends to suppress short-wavelength variations in the slip and results in estimated models that are presumed to be smoothed versions of the true slip distribution [R. L. Parker, *Annu. Rev. Earth Planet. Sci.* 5, 35 (1977)].

23. The 6° difference in orientation between the Pacific-North American relative velocity vector and the strike of the San Andreas fault in central California requires some shortening orthogonal to the strike of the fault [J. B. Minster and T. M. Jordan, in *Tectonics and Sedimentation Along the California Margin*, J. K. Crouch and S. B. Bachman, Eds. [*Soc. Econ. Paleontol. Mineral. Spec. Publ.* 38, 1 (1984)]].

24. J. P. Eaton, M. E. O'Neill, J. N. Murdock, *Bull. Seismol. Soc. Am.* 60, 1151 (1970).

25. Y.-B. Tsai and K. Aki, *ibid.* 59, 275 (1969).

26. The net geodetic moment (cosismic plus postseismic) of the 1985 Morgan Hill earthquake between April and August 1984 equaled 1.8 times the seismic moment [W. H. Prescott, N. E. King, G. Guohua, *Calif. Div. Mines Geol. Spec. Publ.* 68, 137 (1984)].

This ratio increased to 2.3 as of January 1986 (W. H. Prescott, *U.S. Geol. Surv. Open File Rep.*, in press).

27. For this calculation, we use the natural or minimum-length inverse (15, 16). In practice, the natural inverse places nearly all the slip at shallow (2 to 4 km) depth, where the resolution of the network is greatest. Although this calculation is clearly artificial and at variance with the seismic evidence for rupture to depths of at least 10 km, this model does provide a reasonable lower bound on the seismic moment.

28. K. Shimazaki and T. Nakata, *Geophys. Res. Lett.* 7, 279 (1980).

29. A lower bound of 14 km on the transition depth is reasonable because the occurrence of aftershocks to 14 km demonstrates postseismic and, possibly, coseismic slip to this depth. We do not consider transition depths greater than 22 km here because the best-fitting deep-slip rates for these models exceed the long-term slip rate of 33 mm year⁻¹. Time-dependent response to the 1857 earthquake might have caused the deep-slip rate during the 25-year measurement period to lag the long-term rate. We consider it unlikely that the deep-slip rate during this period exceeded the long-term rate, although this possibility is not inconsistent with the data.

30. The inverse that minimizes the squared difference between the estimated and prior models

$$\sum_{i=1}^M (s_i - s_i^{\text{prior}})^2$$

where s^{prior} is the prior model, can be calculated from the natural inverse (15, 16) after a change of variables (31).

31. C. L. Lawson and R. S. Hanson, *Solving Least Squares Problems* (Prentice-Hall, Englewood Cliffs, NJ, 1974).

32. The ambiguity in rigid body motions involved in calculating station velocities from relative length changes [W. H. Prescott, *J. Geophys. Res.* 86, 6067 (1981)] were removed by finding the rigid body translation and rotation that minimized the discrepancy with the predicted velocity field.

33. We thank W. Ellsworth, J. Langbein, M. Matthews, W. Menke, D. Oppenheimer, W. Prescott, J. Savage, R. Simpson, and W. Thatcher for advice and thoughtful reviews of the manuscript.

10 March 1986; accepted 24 June 1986

Abnormal Polarity of Thunderclouds Grown from Negatively Charged Air

C. B. MOORE, B. VONNEGUT, T. D. ROLAN, J. W. COBB,
D. N. HOLDEN, R. T. HIGNIGHT, S. M. MCWILLIAMS,
G. W. CADWELL

Experiments were carried out in New Mexico to determine whether the electrification processes that lead to the formation of lightning in clouds are influenced by the polarity of the charges in the air from which the clouds grow. The normal, positive space charge in the sub-cloud air was reversed by negative charge released from an electrified wire, suspended across a 2-kilometer-wide canyon. On more than four occasions when the clouds over the wire grew and became electrified, they were of abnormal polarity with dominant positive charges instead of the usual negative charges in the lower part of the cloud. The formation of these abnormally electrified clouds suggests both that the electrification process in thunderclouds can be initiated and that its polarity may be determined by the small charges that are present in the atmosphere.

ALMOST AS SIGNIFICANT AS BENJAMIN Franklin's demonstration that lightning is a form of electricity is his observation "that the clouds of a thunder-gust are most commonly in a negative state of electricity, but sometimes in a positive state" (1, p. 42). Electrical measurements that have since been made all over the world confirm his finding and show that in nearly all thunderstorms there is a dominant negative charge in the lower part of the cloud. Measurements from airplanes (2) and balloons (3) show that there is usually also a dominant positive charge in the upper part of these clouds.

This strong bias of polarity has important consequences. The upper, positive part of the dipole attracts negative charge from the upper atmosphere to the top of the cloud by conduction. The lower, negative part of the dipole exports negative charge to the earth by lightning and by point discharge. As a result of these processes, the approximately

1000 thunderstorms that are continuously in progress over the earth bring about 1 kA of negative charge from the atmosphere to the earth. This current, as Wilson (4) perceived, is responsible for continuously maintaining a negative charge of about 0.5×10^6 C on the earth and an equal positive charge in the atmosphere.

Modern observations also confirm Franklin's finding that clouds are "sometimes in a positive state." During the usual thunderstorm, negative (downward directed, fine weather) electric fields beneath a cloud occur briefly, just after cloud-to-ground lightning (5), during gushes of heavy rain, and in the dying stage of the storm (6). Occasionally, storms occur that are electrically different from the usual ones. Gunn (7) reported several storms that produced sustained electric fields at the ground comparable in intensity to ordinary storms, but these fields were in the downwardly directed, fine weather direction with dominant positive charge

aloft. This observation shows that the thunderstorm charge distribution can occasionally be the opposite of that usually encountered. Imyanitov *et al.* (8) have reported that the upper parts of some storm clouds have negative instead of positive charge. Data obtained from lightning-detecting networks by Orville *et al.* (9) and Rust *et al.* (10) provide evidence for the existence of storms that are abnormal in that most of the cloud-to-ground discharges bring down positive instead of negative charge (9, 10).

A requirement of any theory of electrification is to explain why, with few exceptions, the electrical dipole in the cloud develops with positive charge uppermost and negative charge below. The various thunderstorm electrification mechanisms proposed can be divided into two classes, depending on the explanations for this charge distribution.

According to the first class, which is based on the so-called "induction," "influence," or "feedback" theories of thunderstorm electrification, the polarity of the dipole is determined by the polarity of weak space charges or electric fields that may be present in the atmosphere during the development of the cumulus cloud before it becomes a thunderstorm. It is possible that a cumulus cloud behaves as a high-voltage influence machine, such as the Kelvin water dropper (11) and similar devices developed later (12). If a cumulus cloud becomes electrified by a similar mechanism, the polarity of the thunderstorm will be determined by the polarity of the weak charges that are carried up into the

C. B. Moore, T. D. Rolan, J. W. Cobb, D. N. Holden, R. T. Hignight, S. M. McWilliams, G. W. Cadwell, Langmuir Laboratory, New Mexico Institute of Mining and Technology, Socorro, NM 87801.
B. Vonnegut, Atmospheric Sciences Research Center, State University of New York at Albany, Albany, NY 12222.